Advanced Functional Materials

ADVANCED FUNCTIONAL MATERIALS
www.afm-journal.de

RESEARCH ARTICLE OPEN ACCESS

Digital Actuation Control of Soft Robotic Origami With Self-Folding Liquid Crystal Elastomer Hinges

David C. Bershadsky[1] | Tuo Zhao[2] | Glaucio H. Paulino[2,3] | Emily C. Davidson[4]

[1]Electrical and Computer Engineering, Princeton University, Princeton, USA | [2]Civil and Environmental Engineering, Princeton University, Princeton, USA | [3]Princeton Materials Institute, Princeton University, Princeton, USA | [4]Chemical and Biological Engineering, Princeton University, Princeton, USA

Correspondence: Glaucio H. Paulino (gpaulino@princeton.edu) | Emily C. Davidson (edavidson@princeton.edu)

Received: 21 September 2025 | **Revised:** 25 February 2026 | **Accepted:** 25 February 2026

Keywords: 3D printing | closed loop control | liquid crystal elastomers | origami | soft robotics

ABSTRACT

Soft robotics has sought to integrate seamless, programmable shape morphing into dynamic, complex structures. We present a design-for-manufacturing focused approach leveraging reversible shape memory materials to create soft-rigid hybrid self-folding origami robots with fully reconfigurable, reversible actuation. Highly repeatable, closed loop, digital actuation control is achieved through integrated Joule heating of liquid crystal elastomer hinges. Embedded heating traces preserve the planar geometry of origami structures while maximizing the accessible range of motion. We introduce a hybrid direct ink write additive manufacturing system that embeds prefabricated sheet materials, such as flexible printed circuit boards, into 3D printed liquid crystal elastomers to create multi-material composite structures. This approach enables streamlined fabrication of durable soft robotic origami structures with integrated and reconfigurable actuation, which demonstrate more than 1500 cycles with minimal performance degradation.

1 | Introduction

Origami offers a vast library of reconfigurable 3D structures that can be folded from sheet materials. Dynamic transitions between folded states enable tunable mechanical properties and complex programmable behavior. These features are particularly advantageous for achieving compact deployment in soft robotic systems [1–7]. Designing foldable and deployable mechanisms for soft robotics is challenging due to limited soft material options. Integrating rigid materials with these soft systems rapidly introduces manufacturing challenges due to material and process compatibility. Current engineering approaches rely on processes such as over-molding, casting, and gluing [8–11]. These approaches are often error and defect prone leading to premature failures. Actuation of similar soft-rigid hybrid structures is similarly limited. The folding of robotic origami is often driven by external motors [12–14], external magnetic fields [15–18], and pneumatic control [19–21]. However, external motors can limit the accessible range of configurations due to mechanical conflicts, while pneumatic and magnetic systems require specialty infrastructure. This work seeks to address these challenges by the fabrication of soft-rigid hybrid origami robots, integrating foreign materials with stimuli responsive reversible shape memory materials. Taking advantage of these stimuli responsive soft materials with embedded localized Joule heating printed circuit board (PCB) substrates, we demonstrate programmable soft robotic behavior with precise closed loop control.

Shape memory materials, such as prestretched polystyrene [4, 22], have been explored to embed actuation directly within soft robotic systems, offering a seamless alternative to external actuators. However, these materials typically lacked reversibility, limiting their usefulness to single-use or disposable actuation tasks. Early reversible self-folding origami utilized thermally controllable

hydrogels to regulate localized swelling, creating mountain and valley folds [23–25], resulting in brittle structures with limited torque output and requiring immersion in a water bath for activation. In contrast, reversible shape memory materials such as liquid crystal elastomers (LCEs) have enabled self-folding origami to achieve high work output in diverse environments [26–30]. Liquid crystal elastomer actuators, when molecularly programmed (through alignment of liquid crystal mesogens), exhibit reversible transitions between an ordered nematic and an isotropic phase. The transition is triggered by heating or cooling the LCE through its nematic-to-isotropic transition temperature (T_{NI}), causing the bulk material to shrink or expand along the nematic director. The nematic director can be programmed through the print direction, which aligns polymer chains through mechanical shearing, extrusion, and sets the nematic director [31–34].

Multi-material direct ink writing (DIW) has enabled the seamless integration of programmed LCE hinges into soft robotic origami through the integration of structural and active materials [26]. These DIW-fabricated systems demonstrate reversible actuation with programmable shape changes such as folding, twisting, and bending [35–37]. Sequential folding has been shown using two distinct liquid crystal elastomers with different actuation temperatures, enabling hierarchical control of folding sequences [26]. However, this sequential behavior requires environmental temperature gradients or global thermal cycling, which limits both spatial selectivity and actuation speed. Consequently, reliance on environmental heating restricts programmability and impedes precise local control, reducing the viability of such systems for responsive, untethered robotics. Recent efforts have addressed this limitation through: (1) core-shell liquid metal heaters, (2) coaxial hollow LCE fibers for fluid circulation, (3) multi-material DIW printing with conductive inks, (4) simple embedded Joule heating devices like integrated copper traces and casting of LCE fibers around coiled wires [38–50]. Core-shell printing enables integrated heating but introduces fabrication complexity and limits the achievable spatial resolution [38]. Similarly, approaches that embed metal wires are often incompatible with DIW techniques, as they disrupt the continuous, layer-by-layer printing process [43]. While simple Joule heating circuits can be integrated, they are rarely used in conjunction with DIW [42], or instead used as a printing substrate rather than being fully integrated into the DIW print [41], limiting geometric complexity and spatial resolution. While current embedded heaters offer improved local control, most implementations restrict the spatial complexity of actuation patterns, limiting the ability to design complex origami behavior in densely packed, multi-joint systems.

We present a new layer-by-layer direct ink writing (LBL-DIW) (Figure 1A) fabrication approach for programmable self-folding soft robotic origami that integrates prefabricated sheet materials — specifically flexible printed circuit boards (Flex-PCBs) — into liquid crystal elastomer (LCE) actuators (Figure 1B) [51, 52]. This method avoids complex multi-material printing by embedding commercial fabricated layer sheets directly into the structure, significantly simplifying fabrication while enhancing functional integration and manufacturing consistency. Flex-PCBs provide highly localized Joule heating, embedded control electronics, and optional mechanical modification, including fiberglass (FR4) stiffeners and adhesive tabs in a single sheet, enabling a streamlined integration of targeted local heating and mechanical panels (Figure 1C). Targeted Joule heating, coupled with large copper dead zones for thermal dissipation, enables greater than two times faster actuation than comparable LCE actuators [31, 50]. Embedded temperature sensors further support precise closed-loop thermal control, allowing repeatable inside-out actuation and eliminating the need for external environmental heating. A unified computer-aided design pipeline automatically generates fold patterns and fabrication files for each subcomponent, ensuring consistent geometry and alignment across the structure [52]. Together, this architecture enables robust, programmable self-folding origami with rapid, highly repeatable actuation control. We present the design, fabrication, and characterization of this system with reconfigurable origami soft-rigid hybrid robots demonstrating fast, repeatable, and controlled closed loop actuation over more than one thousand five hundred cycles with minimal performance degradation.

2 | Results

2.1 | Layer-by-Layer Direct Ink Writing With Programmable Control

Layer-by-layer direct ink writing (LBL-DIW) allows replicable fabrication of origami with integrated programmable actuation control. By embedding flexible printed circuit boards (Flex-PCBs) during layer-by-layer printing, we achieve localized heating for selective actuation, and integrate temperature sensing for closed-loop control. We characterize the performance of LBL-DIW hinge actuators, demonstrate precise control of crease activation sequences, structural reconfiguration, and feedback-control behavior in soft robotic origami systems.

LBL-DIW fabrication enables the integration of flexible printed circuit boards in 3D printed self-folding liquid crystal elastomer origami. Pre-fabricated Flex-PCBs allow targeted Joule heating of individual hinges through integrated circuit design (Figure 1C). The continuous printed circuit board architecture allows for the integration of Joule heaters within each hinge, internal temperature sensing, and large copper dead zones surrounding each fold. These dead zones ensure thermal isolation between hinges, providing large areas for thermal dissipation and minimizing actuation cycle time. This thermal isolation enables selective heating of individual folds. A more extended discussion can be found in the supporting Information, section S1 on 'Thermal Analysis of Localized Joule Heating', and Figure S1. Electrical interconnects between heaters can be designed to simultaneously actuate groups of folds. The number of fold groups is limited only by the number of discrete control channels available (Figure 1B). The groups can be activated in programmable sequences, allowing dynamic fold configurations. This reconfiguration can be used to exhibit programmable robotic behavior, such as the wing flapping of the origami crane (Movie S2). Additionally, reconfiguration enables the encoding of multiple distinct crease patterns within a single structure. LBL-DIW facilitates the incorporation of embedded control electronics, such as temperature sensors, to enable active control of origami actuation. Prefabricated Flex-PCBs can incorporate fiberglass stiffener panels and patterned adhesives. We take advantage of this to integrate structural

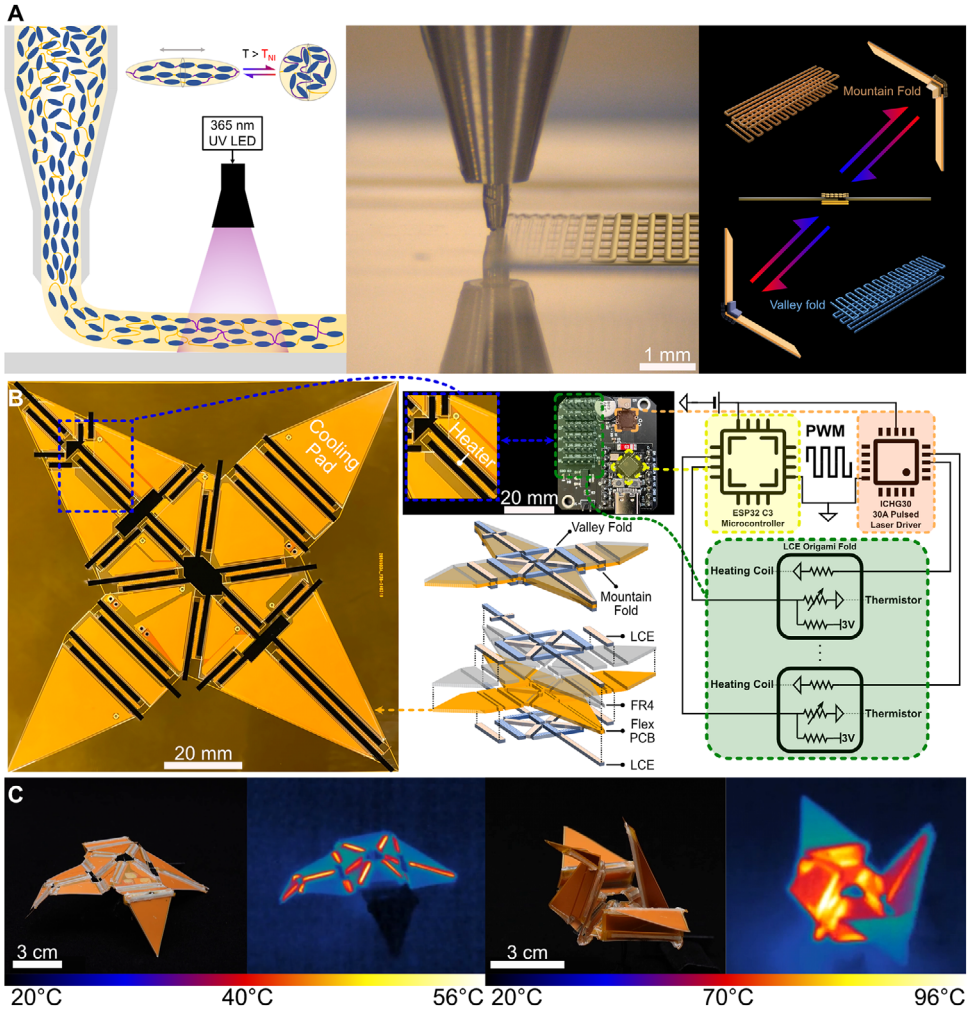

FIGURE 1 | Origami structures: Printing, Design, and Actuation. (A) Direct ink writing of liquid crystalline oligomers creates aligned liquid crystal elastomers along the print direction (left). Sequential layers with orthogonal filaments allow different crease configurations (middle). Mountain and valley folds are defined by the layer ordering (right). (B) Self-folding and programmable actuation is imparted via a flexible printed circuit board (Flex-PCB) (left). The Flex-PCB is embedded within the printed LCE as a structural layer with integrated electronics for Joule heating of individual hinges (middle). A constant current laser driver and microcontroller are used to regulate the power delivered through each hinge, enabling programmable feedback actuation control (right). (C) A self-folding crane is shown going from the unfolded (left) to the folded (right) configuration using integrated Joule heaters. Thermal imagery is pictured in the right subpanel of each figure.

elements of the origami directly into the Flex-PCB substrates. This allows insertion of prefabricated sheets for each layer. Single-step insertion enables complex origami geometries while ensuring consistency between samples.

Previous DIW-fabricated LCE actuators directly integrated LCE hinges, bridging between stiffening panels [26, 51]. However, these approaches are incompatible with embedding Joule heaters inside hinges. To address this challenge, we explored four hinge configurations to determine a proper heater design with minimal impact on fold performance (Figure 2A). To isolate the mechanical impact of the embedded substrate, 127 μm Kapton sheets spanning polyester stiffening panels were used as an analog for flexible printed circuit boards. These Kapton samples were compared to a reference hinge composed of only LCE between polyester stiffening panels. As shown in Figure 2B the serpentine geometry achieved higher bending angles due to its lower bending stiffness. A thinner Kapton substrate was selected for the Flex-PCBs, further lowering the bending stiffness and increasing bending angle; thus this substrate was chosen for our Flex-PCB design. The Flex-PCB, with integrated fiberglass (FR4) stiffeners replacing the polyester panels, and a serpentine configuration demonstrates a torque output similar to the reference hinge under a ~ 1 g load (Figure 2C).

Interfacial adhesion between the printed LCE and the substrate material poses some durability challenges. The selected serpentine geometry ensures full encapsulation of the heating coil within the printed LCE creating a strong mechanical linkage. Adhesion between the edge of the printed LCE and the hinge substrates (Kapton, Polyester, FR4) is important to the durability of the hinge under extended actuation cycles. To ensure a secure linkage, LCE is printed overlapping with the substrate material with a typical overlap of 1 mm, sandwiching the substrate between LCE layers. As seen in Figure 2A the Kapton and polyester samples have visible wrinkles along this interface due to

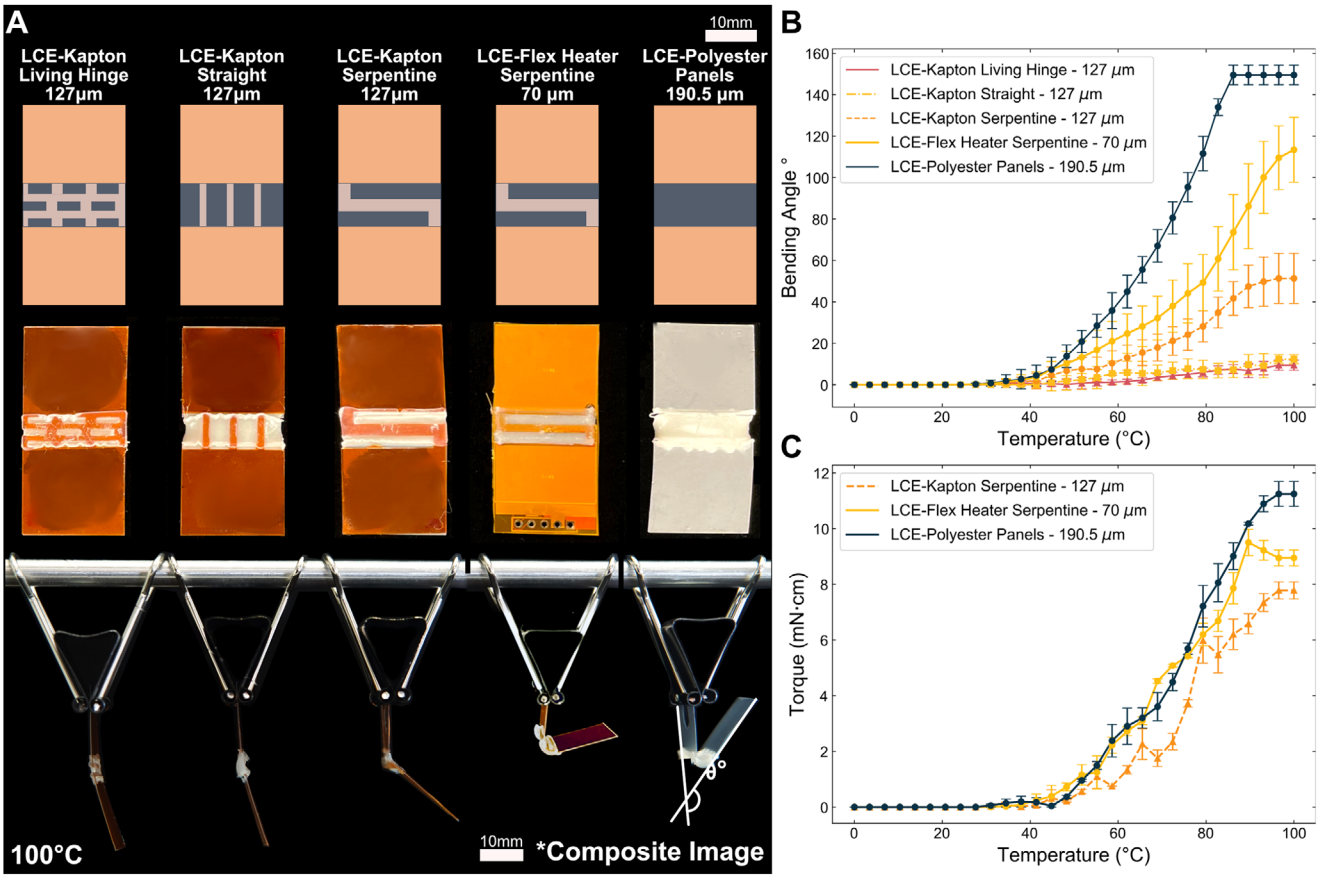

FIGURE 2 | Origami hinge design considering the impact of substrate material and hinge geometry on actuation performance. (A) Four hinge design geometries considered for Flex-PCB design, plus one reference hinge (Top). Printed samples with LCEs (Middle). Hinge actuation at 100°C is displayed for each geometry (Bottom). (B) Bending performance of all five hinge configurations is plotted with a fifth hinge containing only polyester stiffening panels to be used as a reference sample. (C) The output torque of three configurations was characterized by hanging a standard weight from each hinge and extracting the torque value from the angular displacement value. *Composite image: digitally stitched for visual consistency. Statistical methods are shown in the supporting Information, section S3 on 'Statistical Methods'.

the LCE pulling away from the edge during actuation. However, the Flex-PCB with FR4 stiffener sample does not experience this delamination. This improved interfacial adhesion is attributed to the porous nature of the FR4 fiberglass. A further discussion of interfacial adhesion and durability can be found in the supporting Information, section S2 on "Repeatability, Durability, and Long-Term Stability of LCE Actuation", and, Figure S2.

2.2 | Integrated CAD Workflow for Complex Designs

Due to the complexity of origami patterns, individual programming of hinge tool paths and simultaneous PCB layout is prone to errors. Therefore, we present an integrated computer-aided design workflow that streamlines the creation of shape-morphing origami structures, automatically generating manufacturing outputs, and requiring minimal post-processing, for each LBL-DIW component. We developed a simple design workspace, OriCadLCE, that allows for the definition of multi-layer origami patterns with mountain and valley folds, stiffener panels, and integrated adhesive zones (Figure 3A). An in-depth overview of OriCadLCE can be found in the supporting Information, section S4 "OriCadLCE Usage Overview", and Figure S3. The CAD program automatically generates 3D design previews and 3D printing tool paths. It does so while resolving overlapping hinges and accounting for embedded sheets, such as Flex-PCBs (Figure 3B). Vectorized fabrication files are automatically generated for all elements: including structural outlines, stiffer panels, and Joule heating traces within each hinge. These generated outputs can then be minimally post-processed in a PCB design program to add electrical interconnections, embed temperature sensors, and generate PCB fabrication files (Figure 3C). This unified design space ensures that all components fit perfectly together without mechanical conflicts or collisions during DIW printing and assembly. Further details can be found in the Methods (4.1 Shape Morphing Origami Design - 4.2 LBL-DIW Additive Manufacturing).

Careful software integration of these disparate sub-assemblies facilitates the design of more complicated origami crease patterns, increasing the viability of self-folding LCE origami soft robots. The OriCadLCE design process begins with defining the origami crease pattern as illustrated in Figure 3A. The crease pattern consists of multiple elements: LCE mountain and valley folds, structural outlines/cutouts, and modifiers applied to the top and bottom surfaces like stiffening panels and adhesive tabs. After the fold pattern is defined, the

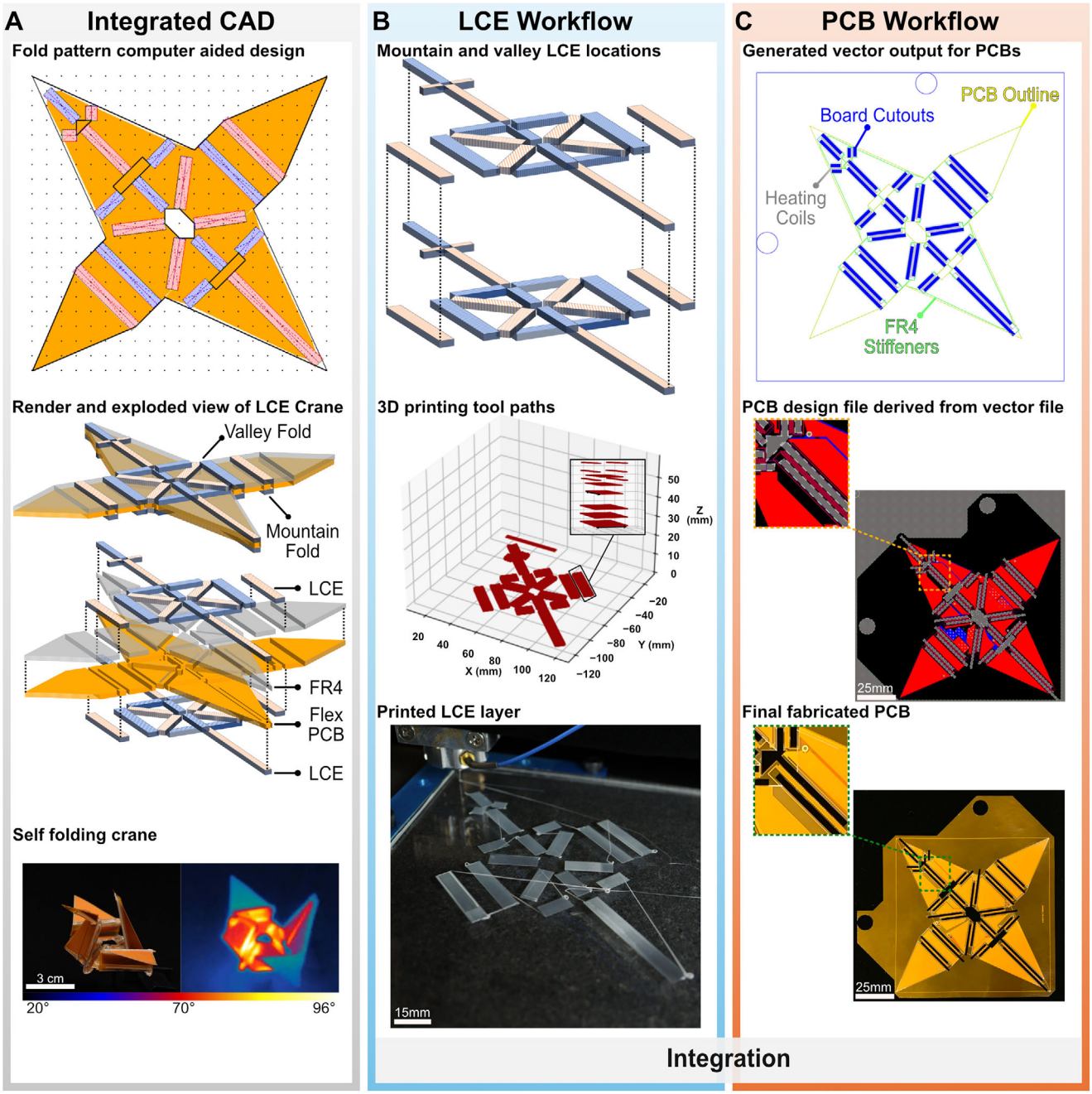

FIGURE 3 | Integrated Design and Fabrication Workflow. (A) An integrated computer-aided design tool (top) simplifies the design workflow of component layers (middle) from concept to finished origami (bottom), allowing the generation of all related fabrication files using only the origami fold pattern as an input. (B) Mountain and valley fold configurations (top) are used to automatically generate 3D printer toolpaths for LCE deposition, accounting for possible mechanical conflicts with embedded materials (middle). LCE is printed according to the generated toolpaths (bottom). (C) Joule heating trace geometries are automatically generated as vectorized outputs along with stiffening zones (top). These vector files are then imported into a PCB design program to create electrical interconnects between Joule heaters (middle). The resulting Flex-PCB is manufactured with holes that enable alignment during LCE printing (bottom).

workflow splits into two branches: DIW printing and LBL sheet fabrication.

The DIW LCE workflow (Figure 2B) automatically generates DIW tool paths using the mountain and valley fold definitions as inputs, while resolving potential mechanical and tool path conflicts with nearby components. A print path preview is displayed, and the output toolpaths are used directly to print the LBL-DIW origami with automatic pausing for insertion of LBL sheets. The LBL sheet (PCB) workflow is very similar but requires minimal post-processing to define electrical interconnects between Joule heating traces. Each distinct attribute (heating traces, stiffeners, adhesives, printed regions, mechanical outlines, and cutouts) of the LBL sheet is exported in a separate vector file in addition to a unified design file with individual layers for each feature (Figure 3C). These vector files can be directly imported into PCB

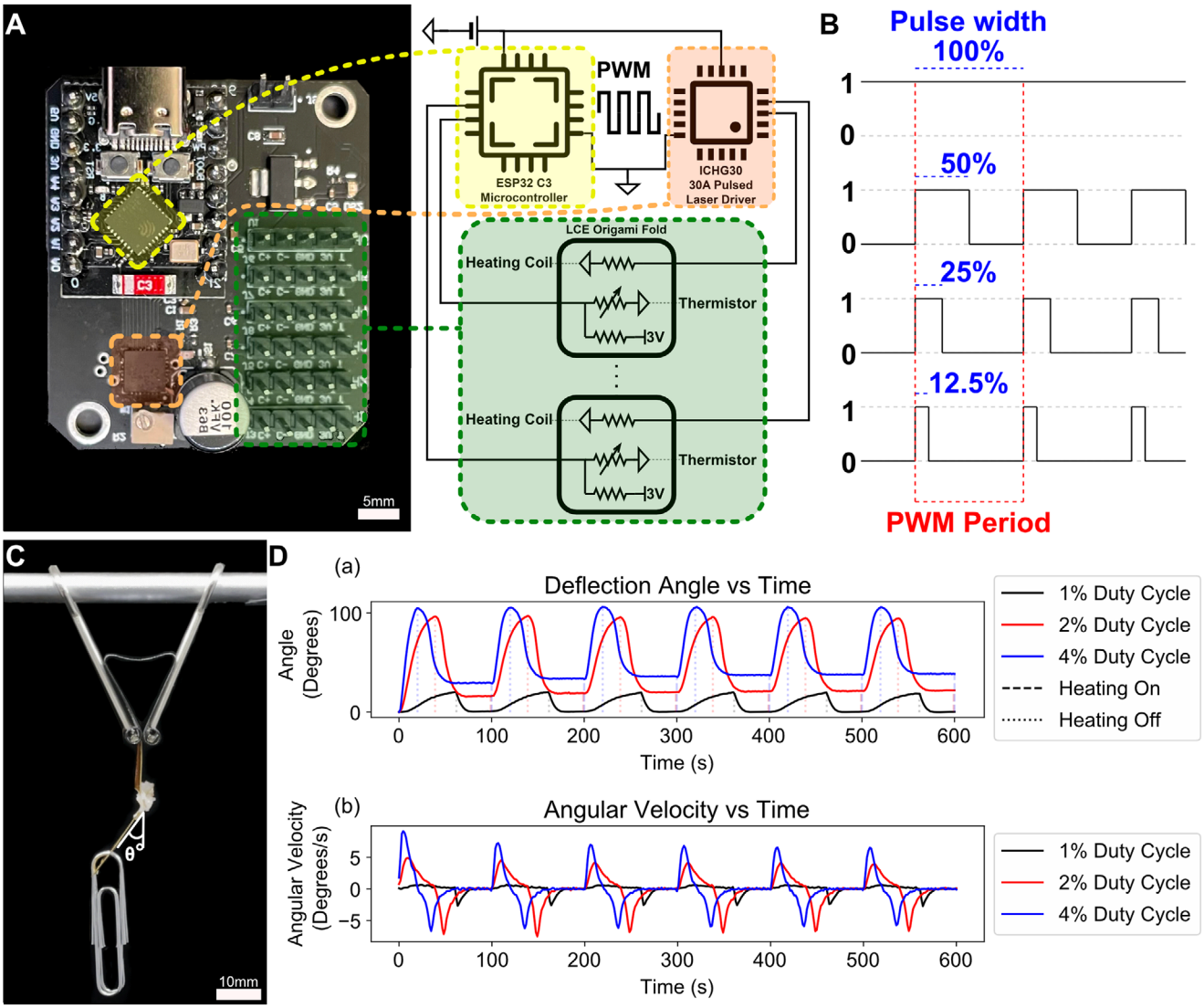

FIGURE 4 | Feedback Control of LCE Hinges. (A) Six-channel constant current driver PCB with wireless microcontroller and Joule heater interface ports (left). Origami Joule heating system diagram (right). (B) Pulse width modulation control allows for precise regulation of power delivered via Joule heating through changes in duty cycle. (C) An LCE origami hinge performing loaded cyclic actuation tests. (D) Cyclic testing over extended periods showed little to no degradation in bending performance after initial cycles.

design software for minimal post-processing and exporting of industry-standard PCB fabrication files. The integration of these two distinct workflows through the embedding of prefabricated sheets during DIW printing enables fabrication of precise and repeatable self-folding origami structures, such as the crane pictured in Figure 3A.

2.3 | Digital Actuation Control via Embedded Joule Heaters

Integration of Joule heating within each hinge via a flexible printed circuit board enables sequential control of hinge actuation. Digital hinge control was achieved via a wirelessly enabled microcontroller combined with a high-power constant current pulsed laser driver, regulating current to the Joule heating hinges (Figure 4A; Figures S4 and S5). Pulse width modulation (PWM) control from the microcontroller determines the current output of the laser driver on each of its six channels (Figure 4B). This provides fine control over the power delivered to each hinge during actuation by modulating the dissipated power. The dissipated power is defined as $i \times V \times dutycycle = P$, where i is current (typically 0.3 A), V is voltage (typically 5 V), and $dutycycle$ is the percentage of each pulse width when the heating is on. Fixed duty cycle cyclic actuation with three distinct PWM values was performed, monitoring both bending angle and angular velocity over time (Figure 4C,D, Movie S1). Little to no degradation in overall bending angle was visible throughout this initial testing. There was, however, some decrease in peak angular velocity as the test continued due to thermal saturation. Once the system was given time to thermally equilibrate, it returned to its initial performance. A full cycle time of 100 s was demonstrated, with excess time to ensure uniform cooling of the hinge. The demonstrated cycle time is more than two times shorter than comparable electrically driven LCE actuators, reducing cycle times from 200 – 300 s to less than 100 s and is an

order of magnitude faster than environmental actuation methods [31, 50]. Additional testing of the hinge with a 2 g load was also performed. Under load, the hinge showed a decrease in peak angle and angular velocity. Further discussion on the behavior of actuators under load can be found in the supporting Information, section S5 on "Actuation Performance Under Load", and Figure S6.

Embedded temperature sensors are used to monitor the thermal state of each hinge (where installed). This built-in temperature monitoring is then used to implement proportional-integral-derivative (PID) feedback control of origami folds. PID feedback control was characterized on a single hinge to understand the mechanical response of the system to the control loop. Given a measured hinge resistance of 3.2Ω and operating voltage of 5 V the maximum current is given by $\frac{5\,V}{3.2\,\Omega} \approx 1.56\,A$. Given this, the PID coefficients (KP: 6.0, KI: 0.2, KD 2.0) were chosen for the system to achieve a fast response with minimal overshoot. The sum of the control terms derived from the error and coefficients was clipped from 0 (off) to 255 (100% duty cycle) and applied to the PWM controller. To assess the performance of the controller, a series of step responses ramping from 25°C to 100°C was performed. At each step, the controller waited a set hold time before continuing to the next setpoint. Both 10 s and 60 s holds were tested (Figure 5A). With the 10 s hold the hinge does not have sufficient time to stabilize at each temperature, resulting in a continuous bending motion. At 60 s there is sufficient time for equilibration and a stair step response is observed. The instantaneous power draw and total power consumed during each test is shown in Figure 5A. Given the proximity of the temperature sensor to the heater and the high speed of the temperature change it was decided to limit the PWM output values to a set of lower thresholds (0–20% and 0–30%) to allow the hinge movement to more closely follow the temperature. This choice slows the response of the system in exchange for more precise movement control.

Using the new PWM limits, cyclic endurance testing was performed. Sets of one hundred sequential step response cycles were carried out. The first set of cycles was performed from 30 to 100°C with a 0%–20% duty cycle cap. The subsequent sets were performed from 30°C to 120°C with a 0%–30% duty cycle cap. Across all one thousand five hundred-plus actuation cycles of the test, no perceptible performance degradation was observed to the naked eye after the initial cycles (Figure 5B). In early cycles, a slight drop off in actuation range was observed, eventually reaching an asymptote, defining the actuator break-in period (Figure 5C). Visual comparisons of the initial and final actuation cycles in Figure 5D do not show a noticeable difference in actuation range. The lack of a major visual discrepancy in actuation performance may be due to a tracking artifact. Motion capture without high-visibility markers on the sample is prone to target drift, which is usually most pronounced early in the data collection. This drift occurs until the target wanders into a locally stable tracking point. Perturbations such as large vibrations of the camera can dislodge the target from the local minimum, causing additional drift. The slight downward drift of the bending angle range in Figure 5B is due to the tracking point sliding inward from the tip of the hinge. Despite this shift, the range of the fifty-cycle excerpt remains approximately constant throughout. Continuous video data was not collected due to storage constraints, with later cycles analyzed via periodic still images. The entirety of the collected endurance data can be found in (Data S1). The test was discontinued due to time constraints; the cycle count at failure remains unknown. Over the course of the fifty cycles featured in Figure 5B, a total of ≈ 1.3 Wh was consumed. With this power consumption, the hinge could be continuously cycled for 2.85 h on a 1000 mAh one-cell lithium battery. This low power consumption is ideal for untethered soft-rigid hybrid robot operations. Some fluctuations in angular velocity were observed throughout the endurance test. These fluctuations were correlated directly with temperature changes in the environment during the experiment. This fully integrated control and sensing scheme allows rapid and repeatable digital actuation control of individual hinges. This precise control enables programmable actuation sequences between distinct states for robotic behavior.

2.4 | Self-Folding Origami for Programmable Crease Patterns

Origami with addressable hinges allows programming of distinct configurations using crease activation sequences. For instance, we fabricated two reconfigurable origami robots via this approach. The first, a self-folding origami crane, was made with individually articulated wings and body (Figures 6 and 7; Figure S7). The second, a Miura sheet, transitions from a standing box to a fully developed Miura–Ori sheet (Figure 7). The crane demonstrates sequential activation, first heating its body, causing shape morphing within the central structure and head. Subsequent heating of both wings simultaneously and continued heating of the body deploy the crane to the fully folded configuration. All three of these heating zones can be independently controlled to individually flap the crane's wings up and down, illustrating complex digital actuation control featured in Movie S2. Reconfigurable self-folding origami is illustrated through a sheet capable of transforming first to a standing box, to a hybrid intermediate state, and then to a full Miura–Ori sheet configuration. The use of three independent heating zones allows the sheet to transition between four distinct configurations. Heating the two perimeter zones, the sheet transforms into the standing box. Heating the main zone along with one perimeter zone reconfigures the structure into a fully developed Miura–Ori sheet. Heating of the main zone while cooling the perimeter zones locks the Miura sheet into an intermediate state between the box and Miura configurations. Individually articulated actuation zones and fold pattern programmability lay the groundwork for fully reconfigurable origami soft robots with complex geometric transformations between folded states.

3 | Conclusion

This work demonstrates the design and fabrication of self-folding origami soft robots that exhibit digitally actuated dynamic reconfiguration between multiple states. Embedded flexible printed circuit boards facilitate integrated Joule heating. This Joule heating enables closed loop on-demand actuation without depending

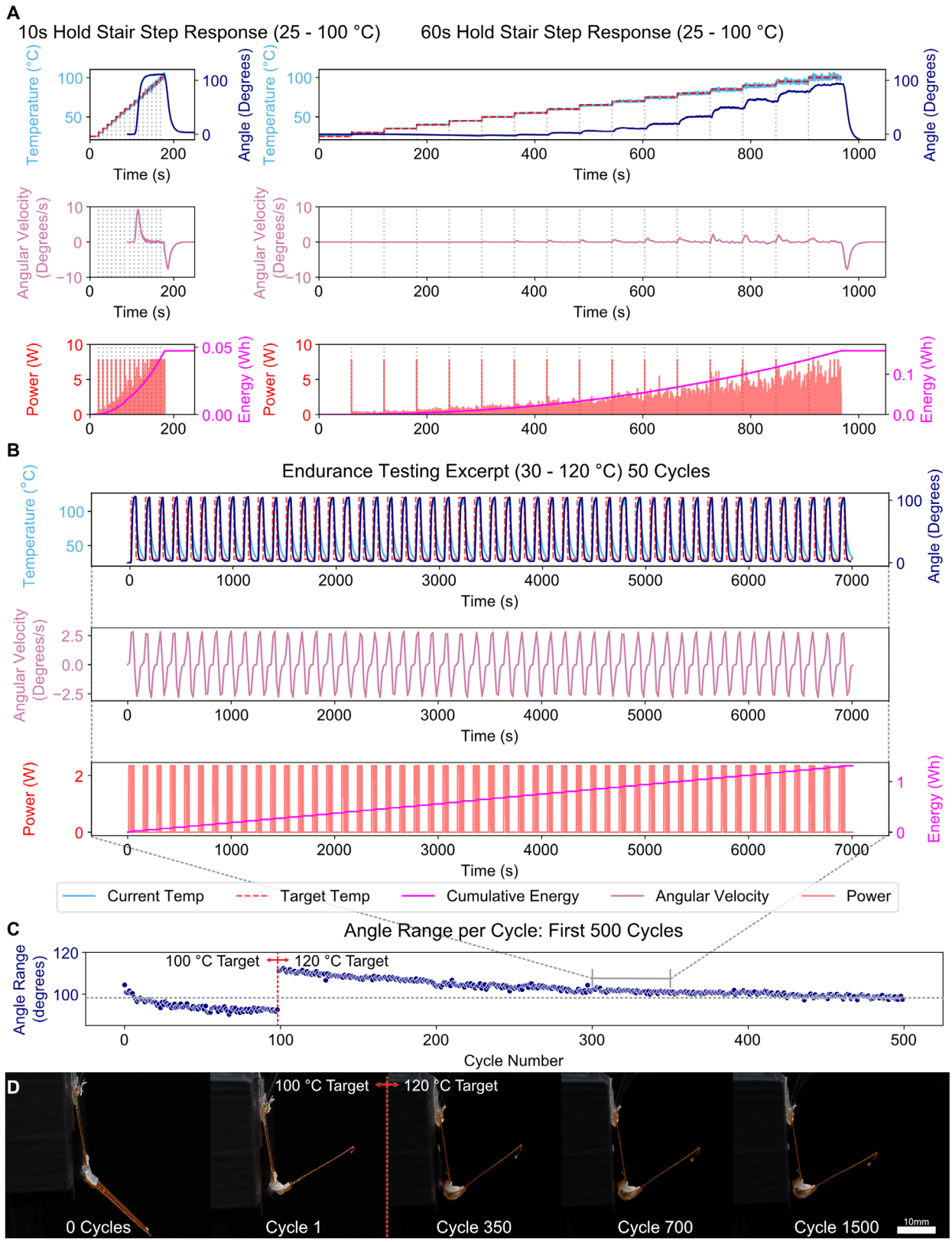

FIGURE 5 | PID Control and Endurance Testing of LCE Hinges (**A**) Two step response stair cases tests are shown from 25 to 100°C. The first features a 10-s hold at each setpoint and the second holds for 60 s. Each plot in the first row contains measured temperature (sky blue), setpoint (red), and deflection angle (navy). The second row contains the angular velocity (mauve), and the third contains instantaneous power draw (red) and total power consumption (fuchsia). (B) An excerpt of 50 cycles, from a more than 1500-cycle endurance test is shown. The coloring is consistent with (A). (C) The actuation range is plotted for each cycle in the first 500 cycles. (D). Image excerpts from the endurance test are pictured at 0 cycles, 1 cycle, 350 cycles, 700 cycles, and 1500 cycles.

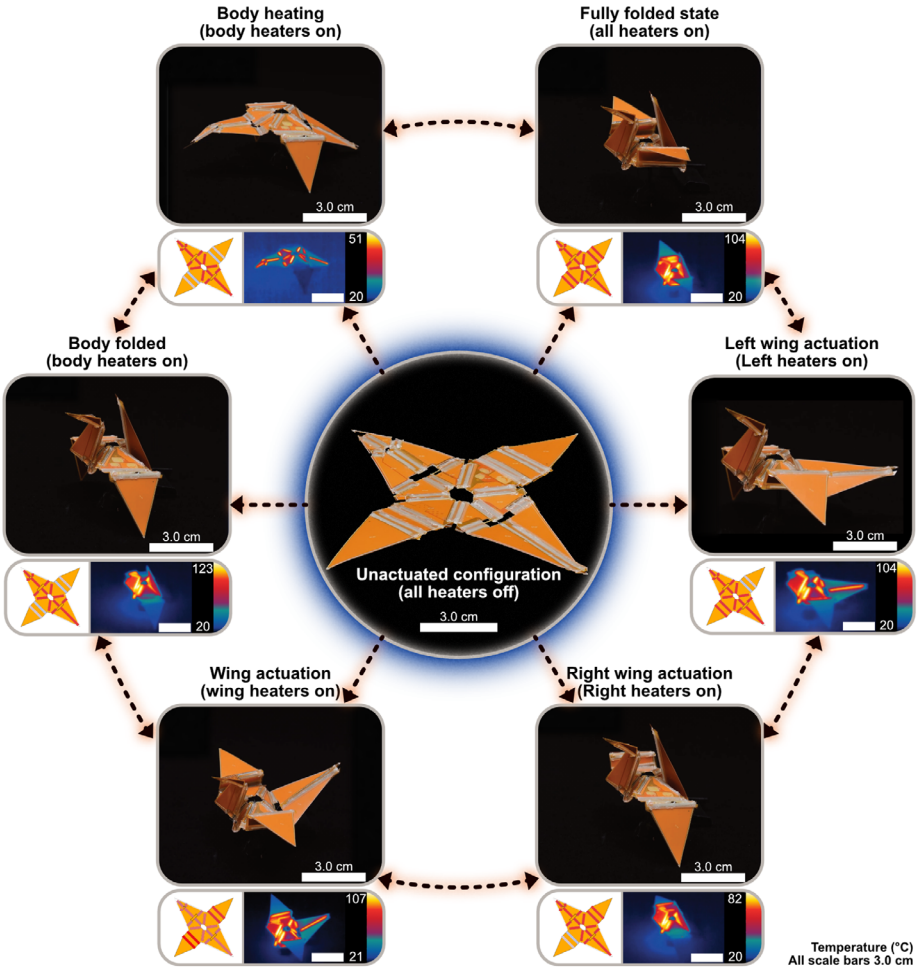

FIGURE 6 | Origami Crane State Space Diagram. The state space diagram illustrates the distinct configurations that the self-folding crane can achieve. The figure also illustrates how the crane is capable of dynamic programmable behavior, such as flapping its wings through targeted actuation control. The inset provides an active heater diagram along with thermal imaging of the origami.

on environmental stimuli such as external temperature gradients. In addition, the Joule heated LCEs achieve sufficient torque output to perform complex shape transformations in air. Simultaneously, the origami actuators show little to no degradation in over one thousand five hundred cycles after some initial cycles. We illustrate examples of programmable robotic behavior through the independent actuation of the body and wings of an origami crane, as well as through the encoding of multiple distinct crease patterns in a Miura sheet. The LBL-DIW design approach enables a straightforward workflow for transforming origami crease patterns into shape-morphing soft-rigid hybrid robotic structures. This work significantly expands the soft-rigid hybrid origami design space. Future work integrating the microcontroller, constant current drivers, and batteries directly onto the Flex-PCB would open the door to untethered, programmable actuation within origami soft-rigid robots. Ultimately, we envision that the approach articulated here could enable low cost, high throughput, and highly replicable fabrication of self-folding origami. The creation of such standardized self-folding origami 'unit cells' could be utilized for the creation of dynamically reconfigurable metamaterials as well as the creation of 'swarms' of robotic unit cells with emergent behaviors [53, 54].

4 | Experimental Methods

4.1 | Shape Morphing Origami Design

Design of origami begins with defining the origami crease pattern in OriCadLCE and assigning a fold width to each crease. The design of LCE origami patterns is explored in more detail in the supporting Information, section S4 on "OriCadLCE Usage Overview" and Figure S3. The expansion of creases into folds results in unphysical overlaps at tight vertices. To resolve this issue, OriCadLCE automatically adjusts the length of each fold, minimizing conflicts. Folds can be assigned to both mountain (red) and valley (blue) hinges, allowing folding in both directions. Next, structural elements are added to the design, including stiffener panels, adhesive tabs, and embedded electronics. Similar conflict resolution is applied to the structural elements as with the folds, preventing overlaps. Each element is assigned a height and thickness. These parameters are used during tool path generation to prevent collisions between the printer nozzle and embedded structures. Automatic tool path generation takes intrinsic print parameters (nozzle diameter, velocity, flow rate) as inputs along with the OriCadLCE design and outputs a complete set of printer instructions with automatic pausing where required for sheet

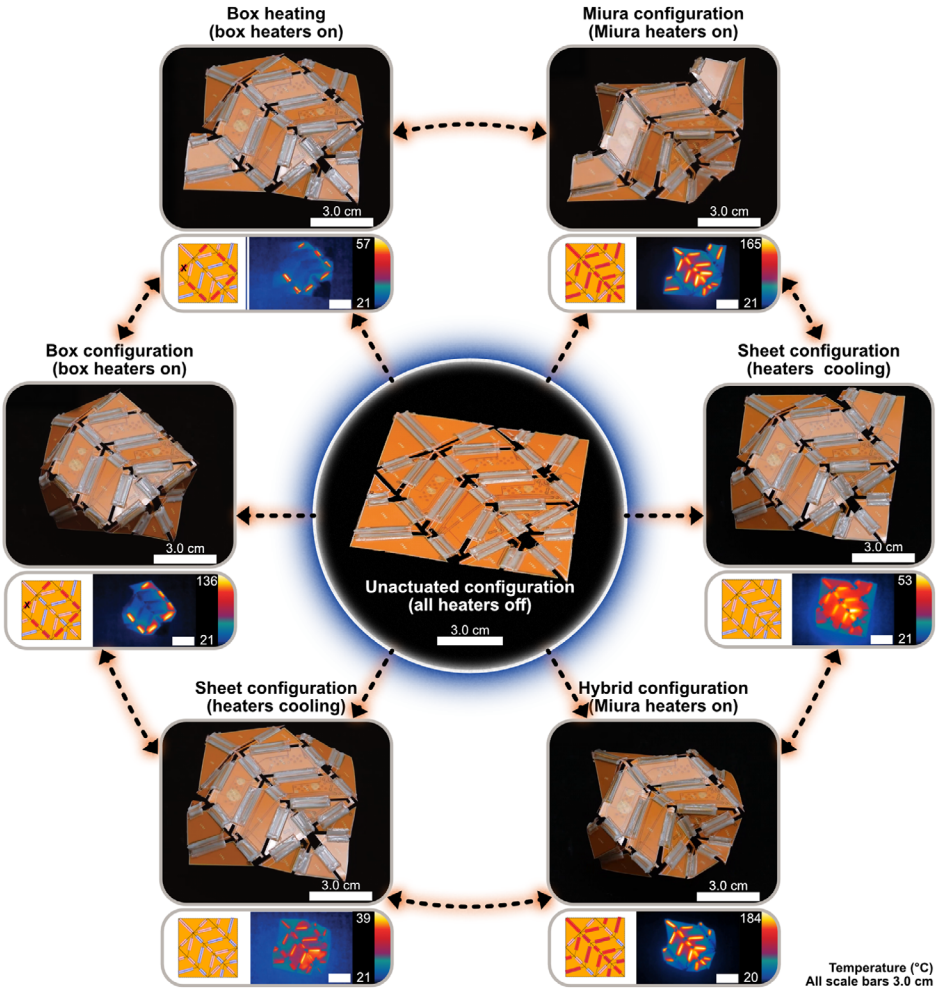

FIGURE 7 | Re-configurable Miura Sheet State Space Diagram. The state space diagram shows the distinct configurations accessible by the re-configurable Miura sheet. The diagram is arranged in a sequential configuration showing how time and thermal-dependent sequencing of actuation can allow access of a unique intermediate configuration (hybrid configuration) while also accessing predefined patterns according to the heating circuits. The inset provides an active heater diagram along with thermal imaging of the origami.

insertion using a fork of the Mecode scriptable gcode library [55]. 3D previews of both the final origami and tool paths are generated for inspection. Structural elements, including those designed by the user (stiffeners, adhesives, and mechanical outlines), and those generated by OriCADLCE (Joule heating traces and fold substrate geometries) are exported in the form of vectorized DXF files. A monolithic design file is created for each layer along with individual files for each structural element. The combined file is imported into a PCB design workspace with each element assigned to its own layer. Electrical interconnects between the Joule heating coils for each fold are manually defined as desired. Finally, standard GERBER fabrication files can be exported for Flex-PCB (Table S1).

4.2 | LBL-DIW Additive Manufacturing

LBL-DIW printing is done via an Aerotech three-axis CNC motion platform equipped with a mechanically driven temperature-controlled barrel extruder. The LCE ink is extruded at 40°C through a 250 μm tapered nozzle (Tecdia). Detailed printing parameters can be found in Table S3. Shear and extensional forces during printing align the liquid crystal mesogens along the direction of flow. Liquid crystal layers are printed in orthogonal orientations to induce bending in mountain and valley hinge configurations. Between LCE layers, prefabricated LBL Flex-PCB sheets are inserted and aligned using fixed mechanical alignment pegs. The LBL sheets are encapsulated within the structure as subsequent LCE layers are printed. After printing, the entire structure is placed in a UV chamber at 365 nm using a ThorLabs M365L3 LED source with collimating lens, yielding approximately 35 $mWcm^{-2}$ for approximately one hour per side to crosslink. To verify expected LCE alignment, single layer LCE samples were printed and actuated. A contraction ratio of about 0.42 was observed (Figure S8), which correlates to an order parameter of 0.46 (Figure S9). An order parameter of ~ 0.45 is typically the maximum observed for DIW printed LCEs [34].

4.3 | LCE Synthesis

The liquid crystalline oligomer ink is based on the C6M liquid crystal mesogen (also called RM82) following a previously

described synthesis [51]. A typical synthesis was performed at approximately the 6.5 g scale. 5 grams of C6M mesogen is added to a 30 ml amber vial along with a stir rod. To the vial, 1.331 ml of (ethylenedioxy)diethanethiol (EDDT), 0.1298 g of butylated hydroxytoluene (BHT), 0.1071 ml of triazine-2,4,6-trione (TATATO), 0.0974 g of dimethylolpropionic acid (DMPA), and 0.0894 ml of triethanolamine (TEA) are added. The mixture is then heated at 90°C until the reagents are fully melted. Once melted, the amber vial is vortexed for 1 min ensuring uniform mixing of reagents. The mixture is then placed in an oil bath at 65°C for 24 h. Before printing, TEA is evaporated from the liquid crystalline oligomer via a vacuum oven at 90°C for 1 h per gram of C6M. The prepared ink is stored in a refrigerator for stability until ready for use. A list of chemical suppliers and CAS numbers is provided in Table S2.

4.4 | Digital Actuation Control

Digital actuation control was achieved using a custom-built driver board. A 30 A pulsed laser driver (IC-HG30) module was used to drive up to six Joule heating channels with a maximum of 5 A constant current supply. Typical currents per channel were closer to approximately 2 A. An ESP32-C3 microcontroller was used as a user interface, to collect sensor data, and control the constant current driver. A web-hosted interface enabled the definition of actuation sequences across the six channels using fixed current and time-based control, and temperature feedback control using embedded temperature sensors. Communications between the ESP32 and IC-HG30 were carried out over six independent PWM channels, corresponding to each pulsed constant current output. The IC-HG30's internal pulse width was set to a fairly low duty cycle using external potentiometers to achieve sufficient heating while retaining granular control over heating rate using the much slower PWM interface from the ESP32. For feedback control, a PID control loop was employed using temperature readings collected from embedded thermistors within the Joule heating traces targeting specific temperatures

4.5 | Actuation Testing

Actuation characterization was performed using two methods for this work: integrated Joule heating and passive environmental heating. Actuation of LCE hinges with test materials for LBL layer sheet substrates was performed in an oven cycled from 25°C to 100°C. Bending angles were measured by hand using ImageJ. During Joule heating experiments, 5 V was applied to a test hinge with a given duty cycle, and bending angles were automatically extracted using the ImageJ Photbend plugin [56]. Various substrate materials were tested and compared to a reference hinge design using polyester panels. A focus was placed on Kapton (polyimide) as a substrate material due to its use in flexible printed circuit boards. Various hinge geometries were explored, including a living hinge cutout, and straight rectangular cutouts overlapping the hinge area. Ultimately, a serpentine cutout was found to yield the best actuation with Kapton substrates. Flexible PCB substrates were fabricated using the serpentine cutout geometry. Torque testing of the serpentine Kapton substrate, flexible PCB substrate, and polyester panel reference design were performed by thermal cycling in the oven under mechanical load. Internal Joule heating was used for cyclic actuation testing of the PCB hinge design and all subsequent demonstrations. Motion capture of Joule heated actuation series was carried out in Davinci Resolve Studio 20, using the IntelliTrack Tracker tool. A comparison between IntelliTrack and Photbend motion capture was performed [56]. IntelliTrack was found to produce less noisy data.

4.6 | Shape Morphing Origami Demonstrations

Actuation control of the demonstrations pictured in Figures 6 and 7 was performed with a fixed duty cycle of 100% and fixed voltage of 15 V with a variable current based on the resistivity of the connected circuit. Imaging of the samples was done simultaneously via a Sony $\alpha 7$ camera and FLIR A400SC, providing both actuation state and thermal information. Samples were suspended in front of a black felt background on soft felt pillars and anchored by the electrical connections on the underside.

4.7 | Wide-Angle X-Ray Scattering

Wide-Angle X-ray Scattering (Transmission) was performed using a GANESHA 300 XL instrument. Data was collected for 10 min at room temperature under vacuum conditions using a Cu Kα beam source ($\lambda = 1.542$ Å). The scalar orientational order parameter $S = \langle P_2(\cos\chi)\rangle$ was calculated from the mesogen peak intensity (from $q = 1.26$ to $q = 1.39$ Å^{-1}) as a function of azimuthal angle χ.

Author Contributions

Author contributions are described below: Conceptualization: DCB, GHP, ECD. Methodology: DCB, TZ, GHP, ECD. Software: DCB. Visualization: DCB. Data curation: DCB. Formal analysis: DCB, TZ, GHP, ECD. Funding acquisition: DCB, ECD, GHP. Supervision: TZ, GHP, ECD. Writing – original draft: DCB, TZ, GHP, ECD. Writing – review and editing: DCB, TZ, GHP, ECD.

Acknowledgments

We thank Katrina Gingell for preliminary work on developing earlier methods for LCE origami printing, Hannah Kim for assistance with LCE printing optimization, and Emily Ostermann for assistance with LCE synthesis. We thank Alice S. Fergerson and Kirstin Bode for supervisory assistance in the lab, and Kelen Ducey for technical assistance with imaging and videography. We thank Evan Scruggs, Franz. A. Stolpen, Jaechul Ju, and Zachariah Page for assistance with WAXS data collection and SEM imaging utilizing instrumentation at UT Austin's Texas Materials Institute. This research was supported by Princeton University Electrical and Computer Engineering Department Kamran Rafieyan '89 Fund for Undergraduate Research (DCB), Princeton University School of Engineering and Applied Science Senior Thesis Funding (DCB), Princeton University Project X Innovation funds (ECD), Princeton Catalysis Initiative funds (GHP), and NSF Grant No. 2323276 (GHP). Additional funding for this research was provided by the NSF Graduate Research Fellowship Program under Grant No. DGE-2137420 (DCB).

Conflicts of Interest

The authors declare no conflicts of interest.

Data Availability Statement

All datasets supporting the findings of this study are openly available in a Princeton Data Commons repository (https://datacommons.princeton.edu/discovery/catalog/doi-10-34770-q55n-0m58). A readme.md and readme.txt file with descriptions of each file are included.

References

1. C. Chen, P. Shi, Z. Liu, et al., "Advancing Physical Intelligence for Autonomous Soft Robots," *Science Robotics* 10, no. 102 (2025): eads1292.

2. E. T. Filipov, G. H. Paulino, and T. Tachi, "Origami Tubes with Reconfigurable Polygonal Cross-Sections," *Proceedings of the Royal Society A: Mathematical, Physical and Engineering Sciences* 472, no. 2185 (2016): 20150607.

3. S. Felton, M. Tolley, E. Demaine, D. Rus, and R. Wood, "A Method for Building Self-Folding Machines," *Science* 345, no. 6197 (2014): 644–646.

4. S. Felton, M. Tolley, B. Shin, et al., "Self-Folding with Shape Memory Composites," *Soft Matter* 9 (2013): 7688–7694.

5. M. E. W. Nisser, S. M. Felton, M. T. Tolley, M. Rubenstein, and R. J. Wood, "Feedback-Controlled Self-Folding of Autonomous Robot Collectives," in *2016 IEEE/RSJ International Conference on Intelligent Robots and Systems (IROS)*.

6. K. Johnson, V. Arroyos, A. Ferran, et al., "Solar-Powered Shape-Changing Origami Microfliers," *Science Robotics* 8, no. 82 (2023): eadg4276.

7. E. Hawkes, B. An, N. M. Benbernou, et al., "Programmable Matter by Folding," *Proceedings of the National Academy of Sciences* 107, no. 28 (2010): 12 441–12 445.

8. L. Ren, Z. Wang, L. Ren, Z. Han, Q. Liu, and Z. Song, "Graded Biological Materials and Additive Manufacturing Technologies for Producing Bioinspired Graded Materials: An Overview," *Composites Part B: Engineering* 242 (2022): 110086.

9. R. Andrejczuk, M. Scharff, J. Ni, A. Richter, and E.-F. M. Vorrath, "A Low-Cost Prototype of a Soft–Rigid Hybrid Pneumatic Anthropomorphic Gripper for Testing Tactile Sensor Arrays," *Actuators* 14, no. 5 (2025): 252.

10. U. Culha, J. Hughes, A. Rosendo, F. Giardina, and F. Iida, *Design Principles for Soft-Rigid Hybrid Manipulators* (Springer, 2016).

11. A. Goshtasbi, L. Grignaffini, and A. Sadeghi, "Bio-Inspired 3D Printing Approach for Bonding Soft and Rigid Materials Through Underextrusion," *Scientific Reports* 15, no. 1 (2025): 4429.

12. C. H. Belke, K. Holdcroft, A. Sigrist, and J. Paik, "Morphological Flexibility in Robotic Systems Through Physical Polygon Meshing," *Nature Machine Intelligence* 5, no. 6 (2023): 669–675.

13. P. Bhovad, J. Kaufmann, and S. Li, "Peristaltic Locomotion Without Digital Controllers: Exploiting Multi-Stability in Origami to Coordinate Robotic Motion," *Extreme Mechanics Letters* 32 (2019): 100552.

14. D. Feshbach, X. Wu, S. Vasireddy, et al., "CurveQuad: A Centimeter-Scale Origami Quadruped that Leverages Curved Creases to Self-Fold and Crawl with One Motor," in *2023 IEEE/RSJ International Conference on Intelligent Robots and Systems (IROS)* (2023): 2485–2492.

15. T. Zhao, X. Dang, K. Manos, et al., "Modular Chiral Origami Metamaterials," *Nature* 640, no. 8060 (2025): 931–940.

16. Y. Kim, H. Yuk, R. Zhao, S. A. Chester, and X. Zhao, "Printing Ferromagnetic Domains for Untethered Fast-Transforming Soft Materials," *Nature* 558, no. 7709 (2018): 274–279.

17. S. Miyashita, S. Guitron, S. Li, and D. Rus, "Robotic Metamorphosis by Origami Exoskeletons," *Science Robotics* 2, no. 10 (2017): eaao4369.

18. S. Miyashita, S. Guitron, M. Ludersdorfer, C. R. Sung, and D. Rus, "An Untethered Miniature Origami Robot That Self-Folds, Walks, Swims, and Degrades," in *2015 IEEE International Conference on Robotics and Automation (ICRA)* (2015): 1490–1496.

19. Y. Zhang, T. Tendo, and T. Tachi, "Modular Design of Multistable Pneumatic Structures from a Flat Pattern of Air Pouches," *Journal of the International Association for Shell and Spatial Structures* 64, no. 4 (2023): 298–305.

20. J. T. B. Overvelde, T. A. de Jong, Y. Shevchenko, et al., "A Three-Dimensional Actuated Origami-Inspired Transformable Metamaterial with Multiple Degrees of Freedom," *Nature Communications* 7, no. 1 (2016): 10929.

21. S. Li, D. Vogt, D. Rus, and R. Wood, "Fluid-Driven Origami-Inspired Artificial Muscles," *Proceedings of the National Academy of Sciences* 114 (2017): 201713450.

22. Q. Liu, W. Wang, M. F. Reynolds, et al., "Micrometer-Sized Electrically Programmable Shape-Memory Actuators for Low-Power Microrobotics," *Science Robotics* 6, no. 52 (2021): eabe6663.

23. J. Na, A. A. Evans, J. Bae, et al., "Programming Reversibly Self-Folding Origami with Micropatterned Photo-Crosslinkable Polymer Trilayers," *Advanced Materials* 27, no. 1 (2015): 79–85.

24. J. L. Silverberg, J.-H. Na, A. A. Evans, et al., "Origami Structures with a Critical Transition to Bistability Arising from Hidden Degrees of Freedom," *Nature Materials* 14, no. 4 (2015): 389–393.

25. C. Li, Y. Xue, M. Han, et al., "Synergistic Photoactuation of Bilayered Spiropyran Hydrogels for Predictable Origami-Like Shape Change," *Matter* 4, no. 4 (2021): 1377–1390.

26. A. Kotikian, C. McMahan, E. C. Davidson, et al., "Untethered Soft Robotic Matter with Passive Control of Shape Morphing and Propulsion," *Science Robotics* 4, no. 33 (2019): eaax7044.

27. S. Wu, T. Zhao, Y. Zhu, and G. H. Paulino, "Modular Multi-Degree-of-Freedom Soft Origami Robots with Reprogrammable Electrothermal Actuation," *Proceedings of the National Academy of Sciences* 121, no. 20 (2024): e2322625121.

28. K. Liu, F. Hacker, and C. Daraio, "Robotic Surfaces with Reversible, Spatiotemporal Control for Shape Morphing and Object Manipulation," *Science Robotics* 6, no. 53 (2021): eabf5116.

29. W. Chen, S. Yang, C. Zhu, et al., "Scalable Jet Swimmer Driven by Pulsatile Artificial Muscles and Soft Chamber Buckling," *Advanced Materials* 37, no. 37 (2025): 2503777.

30. S. Xu, X. Hu, R. Yang, et al., "Transforming Machines Capable of Continuous 3D Shape Morphing and Locking," *Nature Machine Intelligence* 7, no. 5 (2025): 703–715.

31. A. Kotikian, R. L. Truby, J. W. Boley, T. J. White, and J. A. Lewis, "3D Printing of Liquid Crystal Elastomeric Actuators with Spatially Programed Nematic Order," *Advanced Materials* 30, no. 10 (2018): 1706164.

32. C. P. Ambulo, M. J. Ford, K. Searles, C. Majidi, and T. H. Ware, "4D-Printable Liquid Metal–Liquid Crystal Elastomer Composites," *ACS Applied Materials and Interfaces* 13, no. 11 (2021): 12805–12813.

33. M. L'opez-Valdeolivas, D. Liu, D. J. Broer, and C. S'anchez-Somolinos, "4D Printed Actuators with Soft-Robotic Functions," *Macromolecular Rapid Communications* 39, no. 5 (2018): 1700710.

34. R. Telles, A. Kotikian, G. Freychet, et al., "Spatially Programmed Alignment and Actuation in Printed Liquid Crystal Elastomers," *Proceedings of the National Academy of Sciences* 122, no. 3 (2025): e2414960122.

35. Z. Wang, Z. Wang, Y. Zheng, Q. He, Y. Wang, and S. Cai, "Three-Dimensional Printing of Functionally Graded Liquid Crystal Elastomer," *Science Advances* 6, no. 39 (2020): eabc0034.

36. X. Zhan, Z. Ran, J. Li, J. Zhu, Z. Zhang, and K.-L. Yang, "Photo-Responsive Liquid Crystal Elastomer Coils Inspired by Tropism Movements of Plants," *Actuators* 14, no. 4 (2025): 171.

37. M. D. Pozo, J. A. H. P. Sol, S. H. P. van Uden, et al., "Patterned Actuators via Direct Ink Writing of Liquid Crystals," *ACS Applied Materials and Interfaces* 13, no. 49 (2021): 59,381–59,391.

38. A. Kotikian, J. M. Morales, A. Lu, et al., "Innervated, Self-Sensing Liquid Crystal Elastomer Actuators with Closed Loop Control," *Advanced Materials* 33, no. 27 (2021): 2101814.

39. M. Li, F. Gholami, L. Yue, et al., "Coaxial-Spun Hollow Liquid Crystal Elastomer Fiber as a Versatile Platform for Functional Composites," *Advanced Functional Materials* 34, no. 42 (2024): 2406847.

40. M. R. Vinciguerra, D. K. Patel, W. Zu, M. Tavakoli, C. Majidi, and L. Yao, "Multimaterial Printing of Liquid Crystal Elastomers with Integrated Stretchable Electronics," *ACS Applied Materials and Interfaces* 15, no. 20 (2023): 24777–24787.

41. Y. Xia, T. Mu, J. Guo, Y. Liu, and J. Leng, "Multifunctional Untethered Soft Machines Driven by 4D Printed Electrically Responsive Actuators," *ACS Applied Materials and Interfaces* 17 (2025): 36059–36068.

42. S. Wu, Y. Hong, Y. Zhao, J. Yin, and Y. Zhu, "Caterpillar-Inspired Soft Crawling Robot with Distributed Programmable Thermal Actuation," *Science Advances* 9, no. 12 (2023): eadf8014.

43. H. Yang, X. Yin, C. Zhang, B. Chen, P. Sun, and Y. Xu, "Weaving Liquid Crystal Elastomer Fiber Actuators for Multifunctional Soft Robotics," *Science Advances* 11, no. 8 (2025): eads3058.

44. J. Sgotti Veiga, M. Reis Carneiro, R. Molter, et al., "Toward Fully Printed Soft Actuators: UV-Assisted Printing of Liquid Crystal Elastomers and Biphasic Liquid Metal Conductors," *Advanced Materials Technologies* 8, no. 15 (2023): 2300144.

45. J. Sun, Y. Wang, W. Liao, and Z. Yang, "Ultrafast, High-Contractile Electrothermal-Driven Liquid Crystal Elastomer Fibers Towards Artificial Muscles," *Small* 17, no. 44 (2021): 2103700.

46. M. J. Ford, C. P. Ambulo, T. A. Kent, et al., "A Multifunctional Shape-Morphing Elastomer with Liquid Metal Inclusions," *Proceedings of the National Academy of Sciences* 116, no. 43 (2019): 21438–21444.

47. M. J. Ford, M. Palaniswamy, C. P. Ambulo, T. H. Ware, and C. Majidi, "Size of Liquid Metal Particles Influences Actuation Properties of a Liquid Crystal Elastomer Composite," *Soft Matter* 16, no. 25 (2020): 5878–5885.

48. M. Zadan, D. K. Patel, A. P. Sabelhaus, et al., "Liquid Crystal Elastomer with Integrated Soft Thermoelectrics for Shape Memory Actuation and Energy Harvesting," *Advanced Materials* 34 (2022): 2200857.

49. T. A. Kent, M. J. Ford, E. J. Markvicka, and C. Majidi, "Soft Actuators Using Liquid Crystal Elastomers with Encapsulated Liquid Metal Joule Heaters," *Multifunctional Materials* 3, no. 2 (2020): 025003.

50. Q. He, Z. Wang, Y. Wang, A. Minori, M. T. Tolley, and S. Cai, "Electrically Controlled Liquid Crystal Elastomer–Based Soft Tubular Actuator with Multimodal Actuation," *Science Advances* 5, no. 10 (2019): eaax5746.

51. K. Gingell, "Programmable Origami Tubes with Temperature Actuation Using Liquid Crystal Elastomers," *Undergraduate Thesis Princeton University* (2023).

52. D. Bershadsky, "Layer-By-Layer Fabrication Framework for Self-Folding Origami for Metamaterial and Robotic Applications," *Undergraduate Thesis Princeton University* (2024).

53. N. Cheney and H. Lipson, "Topological Evolution for Embodied Cellular Automata," *Theoretical Computer Science* 633 (2016): 19–27.

54. H. Yasuda, P. R. Buskohl, A. Gillman, et al., "Mechanical Computing," *Nature* 598, no. 7879 (2021): 39–48.

55. J. Minardi, "jminardi/mecode," https://github.com/jminardi/mecode (2014).

56. S. Chizhik, A. Sidelnikov, B. Zakharov, P. Naumov, and E. Boldyreva, "Quantification of Photoinduced Bending of Dynamic Molecular Crystals: From Macroscopic Strain to Kinetic Constants and Activation Energies," *Chemical Science* 9, no. 8 (2018): 2319–2335.

Supporting Information

Additional supporting information can be found online in the Supporting Information section.

Supporting File 1: adfm74805-sup-0001-SuppMat.pdf.

Supporting File 2: adfm74805-sup-0002-MovieS1.mp4.

Supporting File 3: adfm74805-sup-0003-MovieS2.mp4.